Defective Ru-doped α-MnO$_2$ nanorods enabling efficient hydrazine oxidation for energy-saving hydrogen production via proton exchange membranes at near-neutral pH

Zhipeng Yu [a,b,1], Chaowei Si [c,d,1], Ferran Sabaté [e], Alec P. LaGrow [b,f], Zhixin Tai [b], Vlad Martin Diaconescu [g], Laura Simonelli [g], Lijian Meng [h], Maria J. Sabater [e,*], Bo Li [i,*], Lifeng Liu [a,b,*]

[a] Songshan Lake Materials Laboratory, Dongguan 523808, China
[b] Clean Energy Cluster, International Iberian Nanotechnology Laboratory (INL), Avenida Mestre Jose Veiga, 4715-330 Braga, Portugal
[c] Shenyang National Laboratory for Materials Science, Institute of Metal Research, Chinese Academy of Sciences, Shenyang 110016, China
[d] School of Materials Science and Engineering, University of Science and Technology of China, Shenyang 110016, China
[e] Instituto de Tecnología Química, Universitat Politècnica de València – Consejo Superior de Investigaciones Cienticas, Avenida Los Naranjos s/n, 46022 Valencia, Spain
[f] Scientific Imaging Section, Okinawa Institute of Science and Technology Graduate University, Kunigami-gun, Okinawa 904-0412, Japan
[g] ALBA Synchrotron, Carrer Llum 2-26, Cerdanyola del Valles, Barcelona 08290, Spain
[h] Centre of Innovation in Engineering and Industrial Technology, Instituto Superior de Engenharia do Porto, Instituto Politecnico do Porto, 4249-015 Porto, Portugal
[i] College of Chemistry and Chemical Engineering, ShenYang Normal University, ShenYang 110034, China

ARTICLE INFO

ABSTRACT

Proton exchange membrane water electrolysis (PEMWE) showes substantial advantages over the conventional alkaline water electrolysis (AWE) for power-to-hydrogen (PtH) conversion, given the faster response and wider dynamic current range of the PEMWE technology. However, PEMWE is currently still expensive due partly to the high voltage needed to operate at high current densities and inevitable usage of precious iridium/ruthenium-based catalysts to expedite the slow kinetics of the oxygen evolution reaction (OER) and to ensure sufficient durability under strongly acidic conditions. Herein, we report that ruthenium doped α-manganese oxide (Ru/α-MnO$_2$) nanorods show outstanding electrocatalytic performance toward the hydrazine (N$_2$H$_4$) oxidation reaction (HzOR) in near-neutral media (weak alkaline and weak acid), which can be used to replace the energy-demanding OER for PEMWE. The as-prepared Ru/α-MnO$_2$ is found to comprise abundant defects. When used to catalyze HzOR in the acid-hydrazine electrolyte (0.05 M H$_2$SO$_4$ + 0.5 M N$_2$H$_4$), it can deliver an anodic current density of 10 mA cm^{-2} at a potential as low as 0.166 V *vs.* reversible hydrogen electrode (RHE). Moreover, Ru/α-MnO$_2$ exhibits remarkable corrosion/oxidation resistance and remains electrochemically stable during HzOR for at least 1000 h. Theoretical calculations and experimental studies prove that Ru doping elongates the Mn–O bond and produces abundant cationic defects, which induces charge delocalization and significantly lowers material's electrical resistance and overpotential, resulting in excellent HzOR catalytic activity and stability. The introduction of N$_2$H$_4$ significantly reduces the energy demand for hydrogen production, so that PEMWE can be accomplished under remarkably low voltages of 0.254 V at 10 mA cm^{-2} and 0.935 V at 100 mA cm^{-2} for a long term without notable degradation. This work opens a new avenue toward energy-saving PEMWE with earth-abundant OER catalysts.

1. Introduction

The rapidly increasing energy demand and environmental pollution have stimulated intensive research on clean, efficient and scalable energy systems [1]. To achieve sustainable energy production, power-to-hydrogen (PtH) conversion via water electrolysis using renewable-

---

sourced electricity will be playing a crucial role in the emerging hydrogen (H_2) economy [2–4]. To this end, proton exchange membrane water electrolysis (PEMWE), as an emerging technology, has shown significant advantages over the conventional alkaline water electrolysis (AWE), because PEMWE allows for higher operational current densities, higher energy efficiency, more compact system design, and more rapid system response [5,6]. However, driving the energy-demanding oxygen evolution reaction (OER) under acidic conditions in PEM electrolyzers is nontrivial [7–9], and the electrocatalysts have to suffer from chemical/electrochemical corrosion and associated severe over-oxidation and dissolution, especially at high operational voltage [10,11]. In this case, using acid-stable platinum group metals (PGMs) such as iridium (Ir) usually becomes indispensable, but this not only substantially increases the hydrogen production cost, but also poses a worrisome risk of global Ir supply, particularly considering the planned deployment on hundreds of gigawatts scale [12]. To address these challenges, significant effort has been made to reducing the Ir usage for acidic OER [5,9,13–15] and developing novel non-PGM based OER catalysts [16,17]. However, only incremental progress has been achieved so far.

Accomplishing OER in a strong acid essentially dictates a harsh condition for electrocatalysts to survive. Therefore, it is highly preferable if the anodic reaction may occur under a much milder condition to alleviate the requirements for the materials of OER catalysts and other components. To this end, replacing OER with the small molecule electro-oxidation reaction (SMOR) represents a promising approach, and some attempts have been made recently by adding molecules such as alcohols [18,19], amine [20,21], urea [22,23] or hydrazine (N_2H_4) [24,25] into the electrolyte during water electrolysis. In this way, the onset of anodic reaction can be largely shifted negatively, not only enabling a mild anodic reaction condition but remarkably lowering the demand for electrical energy input and thereby realizing energy-saving H_2 production. For example, hydrazine oxidation reaction (HzOR) in couple with the cathodic hydrogen evolution reaction (HER) have been reported by several groups [25–28] as an energy-saving approach to H_2 production, because the HzOR in theory takes place at a fairly low potential of −0.33 V *vs.* reversible hydrogen electrode (RHE) [29]. By doing so, H_2 production was able to be accomplished at a large current density of 500 mA cm^{-2} at a low voltage of only 0.53 V with good catalytic stability [24]. Nonetheless, nearly all previous works on SMOR + HER for water electrolysis were demonstrated in strongly alkaline media, and such a concept, to our knowledge, has not been implemented yet for water electrolysis under near-neutral conditions, due mostly to the lack of corresponding efficient and stable HzOR catalysts [30–32].

Herein, we report the synthesis of ruthenium-doped α-manganese oxide (Ru/α-MnO$_2$) nanorods (NRs), which show outstanding HzOR performance in near-neutral electrolytes (weak alkaline and weak acid). Advanced transmission electron microscopy (TEM) and synchrotron X-ray absorption spectroscopy (XAS) measurements revealed that the isomorphical substitution of Mn with Ru in the cryptomelane framework of manganese oxide introduces many cationic defects and elongated Mn–O bonds. Density functional theory (DFT) calculations show that these cationic defects can give rise to charge delocalization and thereby significantly reduce the catalyst's electrical resistance and overpotential for HzOR. Consequently, the Ru/α-MnO$_2$ can catalyze the HzOR under weak alkaline conditions (0.05 M H$_2$SO$_4$ + 0.5 M N$_2$H$_4$, pH = 8.3) at 10 mA cm^{-2} under a potential of merely 0.166 V *vs.* RHE, which is 1.687 V lower than that of OER at the same current density. Impressively, the Ru/α-MnO$_2$ was able to continuously catalyze HzOR more than 1000 h with minimal degradation. Furthermore, we demonstrate that by coupling commercial Pt/C catalysts for the HER, we can accomplish overall hydrazine-mediated PEMWE (OHz-PEMWE) under a low cell voltage of 0.254 and 0.935 V at 10 and 100 mA cm^{-2}, respectively, and the OHz-PEMWE can operate at 100 mA cm^{-2} for at least 120 h without obvious degradation. Besides, PEMWE can also be accomplished in weak acid electrolyte (0.225 M H$_2$SO$_4$ + 0.5 M N$_2$H$_4$, pH = 5.9), and show good overall electrocatalytic performance in two-electrode

configuration, which holds great promise for cost-effective H_2 production using PEMWE technology.

2. Experimental section

2.1. Reagents

Potassium permanganate (KMnO$_4$), manganese sulfate monohydrate (MnSO$_4$·H$_2$O) and ruthenium(III) chloride hydrate (RuCl$_3$·xH$_2$O) were acquired from Sigma-Aldrich, Probus S.A. and Johnson Mathey, respectively. Nitric acid (65%, HNO$_3$) - technical grade was bought from Panreac. Nafion® perfluorinated resin solution (5 wt%) and sulfuric acid (H$_2$SO$_4$) were purchased from Sigma-Aldrich. Pt/C (20 wt%) catalysts and Nafion 115 membranes were purchased from Fuel Cell Store. All reagents and materials were used as received without further purification.

2.2. Synthesis of Ru/α-MnO$_2$

The Ru/α-MnO$_2$ catalysts were synthesized via a method reported previously with some modification [33]. Typically, 2.29 g of KMnO$_4$ were dissolved in 40 mL of Milli-Q water, which was then added to a solution of 3.52 g of MnSO$_4$·H$_2$O in 12 mL of Milli-Q water and 1.2 mL HNO$_3$ (65%). Subsequently, 0.242 g of RuCl$_3$·xH$_2$O was added to the above solution. The mixed solution was refluxed at 100 °C for 24 h. The obtained product was centrifuged, washed with water until the pH was about 7, and then dried under vacuum at 100 °C overnight for further use. The α-MnO$_2$ materials were synthesized using the same procedure as described above without the addition of RuCl$_3$·xH$_2$O.
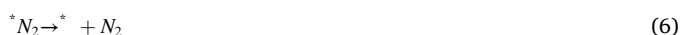
2.3. Materials characterization

Powder X-ray diffraction (XRD) examinations were conducted on an X'Pert PRO diffractometer (PANalytical) working at 45 kV and 40 mA with Cu K$_\alpha$ radiation (λ = 1.541874 Å) and a PIXcel detector. Data were collected with the Bragg-Brentano configuration in the 2θ range of 10 – 80° at a scan speed of 0.01° s^{-1}. X-ray photoelectron spectroscopy (XPS) characterization was performed on an ESCALAB 250Xi instrument with an Al K$_\alpha$ X-ray source (1486.6 eV). Fourier transform infrared spectroscopy (FT-IR) was performed on an ERTEX 80v vacuum FT-IR spectrometer (Bruker). Raman spectroscopy examination was done on a confocal Raman spectrometer (Witec Alpha 300R). Nitrogen adsorption/desorption porosimetry measurements were conducted using a Quantachrome Autosorb IQ2 system at 77 K, and the surface area of samples was derived from the Brunauer-Emmett-Teller (BET) method. The morphology was characterized by scanning electron microscopy (SEM, FEI Quanta 650 FEG microscope equipped with an INCA 350 spectrometer). Transmission electron microscopy (TEM), high-resolution TEM (HRTEM), and scanning transmission electron microscopy (STEM) investigations were carried out on a probe-corrected transmission electron microscope operating at 200 kV (FEI Themis 60 – 300). The actual metal contents of K, Ru and Mn were detected by the inductively coupled plasma – optical emission spectroscopy (ICP-OES, ICPE-9000 spectrometer, Shimadzu). The X-ray absorption spectroscopy (XAS) was conducted at the BL22-CLAESS beamline, ALBA Synchrotron (Barcelona, Spain) [34]. The Si111 and Si311 double-crystal monochromators were exploited to acquire the spectra at the Mn and Ru K-edge, respectively, while the higher harmonics were rejected by choosing the appropriate incident angle and coating for the collimating and focusing mirrors. The XAS spectra were acquired in transmission mode by means of ionization chambers. The X-ray absorption near-edge spectra (XANES) were normalized by the linear representation of the pre-edge subtracted post-edge, while a standard procedure based on the polynomial spline function fit to the pre-edge subtracted spectra was employed to extract the extended X-ray absorption fine-structure (EXAFS) oscillations [35,36]. The Fourier transforms (FTs) were

obtained using a Hanning window in the 3–14 Å^{-1} k range.

2.4. DFT calculations

DFT calculations using the Vienna Ab-initio Simulation Package (VASP) [37,38] were performed to optimize geometry structures, and the projector augmented wave (PAW) [39,40] pseudopotential and Revised Perdew-Burke-Ernzerhof (RPBE) [41] exchange–correlation functional were employed to calculate all geometry optimizations and self-consistent total-energy. Zero damping DFT-D3 method of Grimme was used for van der Waals correlation correction [42]. A kinetic energy cut-off of 400 eV was set for the plane-wave expansion. The convergence criteria of final energy and force of all structures were less than 10^{-6} eV and 0.02 eV, respectively. The Brillouin zone was sampled with $1 \times 1 \times 1$ Gamma k-point mesh for energy and $3 \times 3 \times 1$ Monkhorst-Pack k-point mesh for electronic structure calculations. The α-MnO$_2$ supercell is cubic with dimensions of $19.98 \times 19.98 \times 20.89$ Å^3 for x, y and z directions, and the periodic condition is employed along z direction. The distance between neighbouring cells is 20.89 Å. The following catalyst models were used for the calculations toward the HzOR: pristine α-MnO$_2$; prefect Ru-doped Ru/α-MnO$_2$; Ru/α-MnO$_2$ with cationic defects.

The oxidation of hydrazine into nitrogen and hydrogen occurs via the following six consecutive elementary steps:

$$^* + N_2H_4 \rightarrow {}^*N_2H_4 \tag{1}$$

$$^*N_2H_4 \rightarrow {}^*N_2H_3 + H^+ + e^- \tag{2}$$

$$^*N_2H_3 \rightarrow {}^*N_2H_2 + H^+ + e^- \tag{3}$$

$$^*N_2H_2 \rightarrow {}^*N_2H + H^+ + e^- \tag{4}$$

$$^*N_2H \rightarrow {}^*N_2 + H^+ + e^- \tag{5}$$

$$^*N_2 \rightarrow {}^* + N_2 \tag{6}$$

where the asterisk (*) represents the active site on the model catalysts of pristine α-MnO$_2$, prefect Ru/α-MnO$_2$ and Ru/α-MnO$_2$ with cationic defects. "*N$_2$H$_4$", "*N$_2$H$_3$", "*N$_2$H$_2$", "*N$_2$H", and "*N$_2$" denote the corresponding chemisorbed intermediate species residing on the model catalyst surfaces.

2.5. Electrocatalytic tests

The catalyst ink was prepared by ultrasonically dispersing 5 mg of catalysts into 0.5 mL of isopropanol containing 50 μL of Nafion® solution. To prepare an electrode for catalytic tests, 20 μL of catalyst ink was loaded on a fine-polished glassy carbon (GC) electrode with an exposed area of 0.50 cm^2, leading to a loading mass of ca. 0.36 mg cm^{-2} for the HzOR and OER, respectively. The electrode was then dried at room temperature (ca. 25 °C) naturally in air.

All electrocatalytic tests of half reactions were carried out in a three-electrode configuration at room temperature (23 °C) using a Biologic VMP-3 potentiostat/galvanostat. The catalyst-loaded GC, a graphite rod and a saturated calomel electrode (SCE) were used as working, counter, and reference electrodes, respectively. The OER and HzOR measurements were carried out in 0.05 M and 0.225 M H$_2$SO$_4$. For HzOR tests, different concentrations of hydrazine were dissolved in the electrolyte. The SCE reference electrode was calibrated to the reversible hydrogen electrode (RHE) scale through a method proposed by Jaramillo et al. [43]. In short, clean Pt wires were used as the working and counter electrodes, with the SCE as the reference in the target electrolyte. Cyclic voltammetry (CV) cuves were then recorded at a scan rate of 1 mV s^{-1}, and the potential crossing the zero current was taken as the potential for calibration on RHE scale in subsequent measurements [43].

The apparent OER activity was characterized using CV at a scan rate of 5 mV s^{-1}, and an *iR*-correction (85%) was made to compensate for the voltage drop between the reference and working electrodes, which was measured by a single-point high-frequency impedance test. The electrochemical impedance spectroscopy (EIS) measurements were conducted at 1.853 V *vs.* RHE for the OER and 0.166 V *vs.* RHE for the HzOR in the frequency range of 10^5 – 0.01 Hz with a 10 mV sinusoidal perturbation. The stability of the Ru/α-MnO$_2$ catalyst was assessed using chronopotentiometry (CP) at a constant current density of 10 and 100 mA cm^{-2} for the HzOR. The electrochemically accessible surface areas (ECSAs) were calculated from the electrochemical double-layer capacitance of the catalytic surface according to the following equation [44]:

$$ECSA = \frac{C_{dl}}{C_s} \tag{7}$$

where the double-layer capacitance (C_{dl}) of catalysts was estimated by performing CV in the non-Faradaic potential range of 0.46 to 0.66 V *vs.* RHE at different scan rates (v) of 10, 20, 30, 40, 50, 60, 70, 80, 90 and 100 mV s^{-1}, followed by extracting the slope from the resulting $|j_a - j_c|/2$ *vs.* v plots (j_a and j_c represent the anodic and cathodic current at 0.56 V *vs.* RHE). The specific capacitance value (C_s) was assumed to be 0.035 mF cm^{-2} according to previous studies on metal oxide catalysts [45].

Furthermore, the overall hydrazine-assisted PEMWE was carried out using the Ru/α-MnO$_2$ as the anode catalysts for HzOR and commercially available Pt/C (20% Pt, Fuel Cell Store) as the cathode catalysts for HER. 20 μL of 9.1 mg mL^{-1}Pt/C catalyst ink was loaded on a GC electrode with an exposed area of 0.50 cm^2. The polarization curve was acquired at a scan rate of 5 mV s^{-1} and the stability of PEMWE (i.e., HzOR + HER) was tested at 10 and 100 mA cm^{-2}, respectively. The Nafion® 115 membrane was used in our experiments, which was sandwiched between the anodic and cathodic compartments of a Teflon test cell.

3. Results and discussion

As detailed in the Experimental section, the isomorphically substituted cryptomelane-type Ru/α-MnO$_2$ catalysts were synthesized by a template/surfactant-free reaction between KMnO$_4$ and MnSO$_4$, during which 2 wt% RuCl$_3$ was incorporated drop-wise as the source of Ru dopants. Fig. 1a shows the X-ray diffraction (XRD) patterns of as-prepared Ru/α-MnO$_2$ and the pristine α-MnO$_2$ control sample, which were in good agreement with those previously reported for cryptomelane-type materials, confirming the tetragonal KMn$_8$O$_{16}$ crystal phase (ICDD no. 00–020-0908). No diffraction peaks from any manganese and/or ruthenium segregated phases were detected for Ru/α-MnO$_2$, suggesting that Ru has been successfully doped into/onto the cryptomelane crystallites forming a pure phase. Furthermore, the diffraction peak intensity becomes weaker and the peak position of Ru/α-MnO$_2$ slightly shifts toward a lower angle compared to that of pristine α-MnO$_2$ (Fig. 1a inset), indicating that the Ru doping causes reduced crystallinity and lattice expansion of α-MnO$_2$. The morphology and microstructure of Ru/α-MnO$_2$ and α-MnO$_2$ were further examined by scanning electron microscopy (SEM, Fig. S1) and transmission electron microscopy (TEM, Fig. S2). The pristine α-MnO$_2$ was found to be composed of crystalline NRs, whose diameter and length are 20 – 30 nm and several micrometers, respectively. Doping Ru into α-MnO$_2$ did not markedly alter its NR-like morphology but shortened the length of NRs, as revealed by SEM and TEM examination (Fig. 1b-c and S1), which indicates that the addition of RuCl$_3$ precursors, even little, influences the nucleation and growth of Ru/α-MnO$_2$ NRs. Fig. 1d shows the high-resolution TEM (HRTEM) image, where the interplanar spacing of (310) planes of Ru/α-MnO$_2$ increases from 3.1 Å to 3.7 Å compared to the pristine α-MnO$_2$ (Fig. S2c), consistent with the XRD results. In addition, defective areas with disordered lattice structure were also observed (Fig. 1e), which could be attributed to the substitution of Mn with larger Ru atoms and the variation of Mn valence [46]. Defect
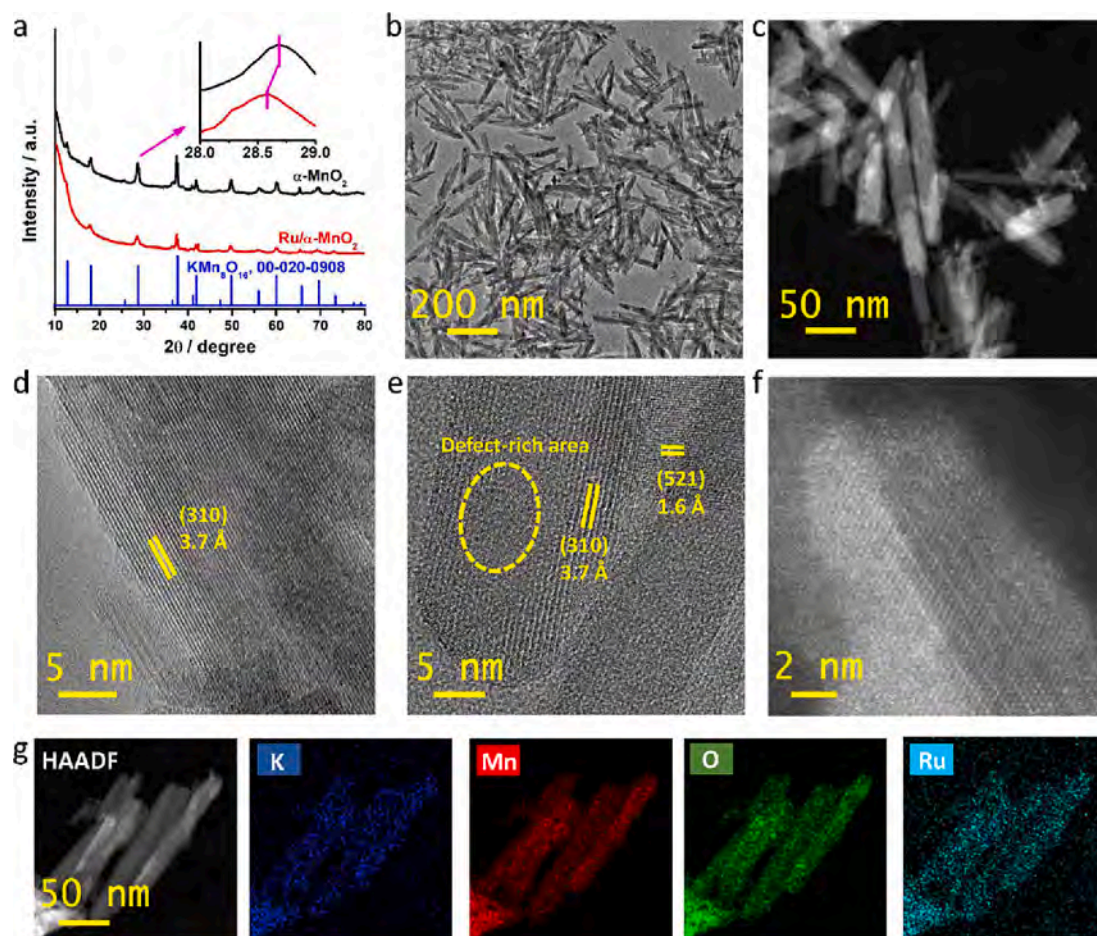
Fig. 1. Morphology and microstructure characterization of Ru/α-MnO₂ catalysts. (a) XRD patterns of Ru/α-MnO₂ and pristine α-MnO₂. (b) Low-magnification TEM image. (c) Low-magnification HAADF-STEM image. (d, e) HRTEM images. (f) HAADF-STEM image. (g) HAADF-STEM image and the corresponding elemental maps of K, Mn, O and Ru.

engineering has been widely used recently to design and optimize microstructure of heterogeneous catalysts [47,48]. Particularly, for metal oxide catalysts, engineering defects, especially cationic defects, turns out to be an effective means to optimize the electronic and orbital structures to create active sites and moderate binding energy with reaction intermediates [49–51].

The incorporation of Ru into α-MnO₂ was further confirmed by inductively coupled plasma – optical emission spectroscopy (ICP-OES) and energy dispersive X-ray spectroscopy (EDS) (Fig. S3 and Table S1). We found that the amount of K nearly remained unchanged after Ru doping, the amount of Mn was reduced, and meanwhile signals from Ru appeared in Ru/α-MnO₂. Therefore, we believe that Ru atoms were doped into the α-MnO₂ structure and expanded the lattice spacing by replacing the Mn atoms located in the framework rather than substituting the K cations in the tunnels, generating disordered amorphous phases [52,53] and inducing a structural disorder [54,55], which was verified by the attenuated XRD peak intensity and broadened full width at half maximum (FWHM, Fig. 1a). According to previous reports [5,33,56], such an amorphous phase comprises a large number of under-coordinated defects, able to boost the electrocatalytic activity and reaction kinetics; moreover, the structurally flexible amorphous phase could also facilitate charge and electron transfer between the active sites and intermediates [22,57]. We further performed aberration-corrected high-angle annular dark-field scanning transmission electron microscopy (HAADF-STEM) to investigate the atomic structure of Ru/α-MnO₂. Given that the HAADF signal intensity is proportional to the square of the atomic number (Z), the bright spots in the HAADF-STEM image

(Fig. 1f and S4) are believed to result from Ru atoms ($Z_{Ru} = 44$ *vs.* $Z_{Mn} = 25$), in agreement with a recent report on Ru/MnO₂ [58]. In addition, elemental mapping showed that the K, Mn, O and Ru elements distribute uniformly along and across the NRs (Fig. 1g). The K element originates from the KMnO₄ precursor used during materials synthesis, which is already incorporated into the lattice of α-MnO₂.

The Fourier transform infrared (FT-IR) and Raman spectra of Ru/α-MnO₂ closely resemble those of pristine α-MnO₂, indicating that introducing Ru atoms into α-MnO₂ did not alter the bulk molecular structure of α-MnO₂ (Fig. S5). However, the Mn–O force constant (*k*) of Ru/α-MnO₂ (299.143 N m⁻¹), calculated from Raman spectra (Fig. S5b) according to the Hooke's Law, was smaller than the original α-MnO₂ (308.564 N m⁻¹), suggesting that the Mn–O bond has been weakened by Ru doping [59–64]. The nitrogen adsorption/desorption isotherm of Ru/α-MnO₂ was further measured and compared to that of pristine α-MnO₂. The Brunauer-Emmett-Teller (BET) specific surface area of the Ru/α-MnO₂ catalysts is 92 m² g⁻¹, substantially higher than that of the pristine α-MnO₂ (61 m² g⁻¹) (Fig. S6), which implies that doping Ru in α-MnO₂ and the induced under-coordinated defects are beneficial to expose more active sites and promote mass transport.

We investigated the surface chemistry of α-MnO₂ and Ru/α-MnO₂ using X-ray photoelectron spectroscopy (XPS). The survey spectrum of Ru/α-MnO₂ shows the presence of K, Mn, Ru, and O elements (Fig. S7), consistent with the above EDS analysis. The high-resolution O1s spectra (Fig. 2a) of all samples can be de-convoluted into several peaks, corresponding to metal–O (529.3 eV), defective O (530.8 eV) and adsorbed water (533.0 eV), respectively [54,65,66]. As shown in Fig. 2a and
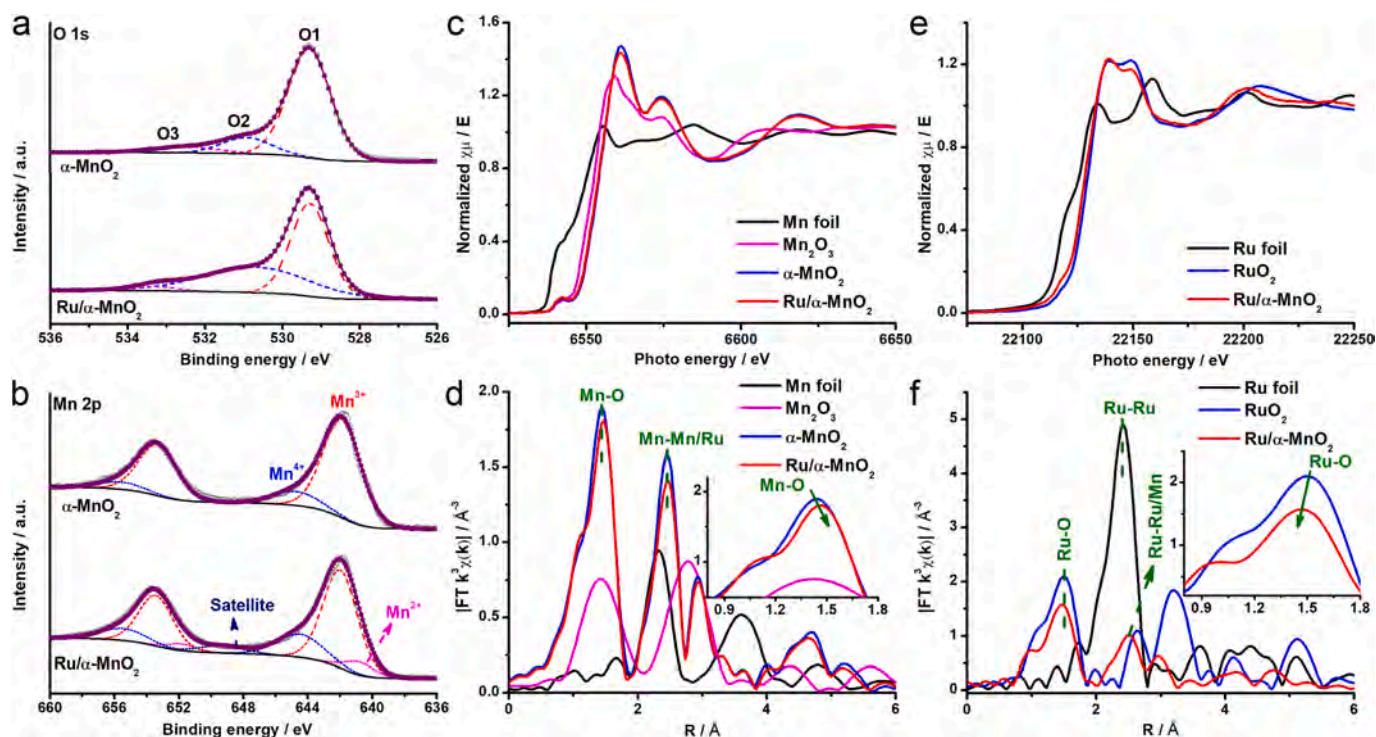
Fig. 2. Electronic structure analyses of Ru/α-MnO₂ and the pristine α-MnO₂. High-resolution (a) O1s, (b) Mn2p XPS spectra of samples. (c) Mn K-edge XANES spectra of Mn foil, Mn₂O₃, α-MnO₂ and Ru/α-MnO₂. (d) Fourier transform of the EXAFS spectra in real (R) space. (e) Ru K-edge XANES spectra of Ru foil, RuO₂ and α-MnO₂. (f) Fourier transform of the EXAFS spectra in real (R) space.

Table S2, the proportion of metal–O bonds in Ru/α-MnO₂ decreases markedly, and Ru/α-MnO₂ possesses more oxygen defects, with respect to α-MnO₂. Besides, the Mn2p spectra of samples are analyzed (Fig. 2b). The α-MnO₂ shows two de-convoluted Mn2p$_{3/2}$ peaks at 641.9 and 644.7 eV, which can be assigned to Mn^{3+} and Mn^{4+} species, respectively [65,67]. For Ru/α-MnO₂, in addition to the contributions from Mn^{3+} and Mn^{4+} species, a new peak that is ascribed to Mn^{2+} (ca. 7.5%) appears, due to the change of valence states of Mn upon Ru doping [60]. Moreover, a weak satellite peak is observed at ca. 649.4 eV, which is the characteristic of Mn^{2+} species [68], corroborating that α-MnO₂ was partially reduced upon Ru doping. Additionally, the high-resolution Ru3p$_{3/2}$ spectrum of Ru/α-MnO₂ was acquired, which displays two peaks at 463.2 and 467.1 eV, respectively, corresponding to Ru^{3+} and Ru^{4+} species (Fig. S8) [67,69].

X-ray absorption near-edge structure (XANES) spectroscopy measurements were further carried out to gain more insight into the chemical state in the bulk. Fig. 2c shows the Mn K-edge XANES spectra of Mn foil, Mn₂O₃, α-MnO₂ and Ru/α-MnO₂. The absorption spectra of α-MnO₂ and Ru/α-MnO₂ are very similar to that of Mn₂O₃ with the rising edge at a higher energy than that of the Mn foil reference, indicating that the oxidation state of Mn in these samples is close to Mn^{3+}. Fig. 2d displays the Fourier transform (FT) of the k^3-weighted χ(k)-function curves of the non-phase corrected Mn K-edge EXAFS spectra. The α-MnO₂ and Ru/α-MnO₂ exhibit two predominant peaks at 1.45 and 2.47 Å, corresponding to the Mn–O and Mn–Mn bonds, respectively [17,70]. In general, the amplitude of oscillation peaks in *R*-space is related to the atomic coordination number and the mean square disorder, and both a lower coordination number and large mean square disorder are reflected by a lower amplitude [54,55,67]. As revealed in Fig. 2d, the amplitude of the characteristic peaks of Ru/α-MnO₂ is smaller than that of α-MnO₂, suggesting the existence of a slightly higher local structural disorder around the Mn site in Ru/α-MnO₂ [25,71]. Additionally, the distance between O and Mn atoms increases after the original Mn atoms are replaced by Ru atoms, consistent with the Raman results (Fig. S5b) [65,71]. The Ru K-edge XANES spectra (Fig. 2e) show

the rising edge of Ru/α-MnO₂ close to that of RuO₂, indicating that Ru in Ru/α-MnO₂ carries positive charges, in agreement with the XPS result (Fig. S8). At Ru K edge, two main features appear in the FT of the EXAFS spectra at 1.46 and 2.50 Å for Ru/α-MnO₂, corresponding to Ru–O and Ru–Ru/Mn bonds, respectively (Fig. 2f) [58]. A closer look at the spectra further discloses that the Ru–O bond in Ru/α-MnO₂ is shorter than that in RuO₂ (inset, Fig. 2f) [65,69], which indicates that after Ru doping, O atoms are "pulled" toward Ru and go away from Mn atoms. This is expected to have an impact on the electrocatalytic performance of sample, as will be discussed later [65,69].

The electrocatalytic performance of Ru/α-MnO₂ catalysts toward HzOR was firstly evaluated in 0.05 M H₂SO₄ electrolyte with different concentrations of hydrazine at a scan rate of 5 mV s^{-1}. As shown in Fig. 3a, within the potential window under investigation (i.e., 0 – 1 V *vs.* RHE) there is no oxidative current appearing in the linear sweep voltammetry (LSV) curve for the electrolyte without hydrazine (black trace in Fig. 3a), while a remarkable oxidative current can be observed as long as 0.1 M N₂H₄ is added into the electrolyte. The anodic current density keeps increasing with the increased concentration of N₂H₄ and finally becomes constant when the N₂H₄ concentration reaches 0.5 M, which is selected as the optimal concentration in our study. In addition, varying the scan rate from 5 to 100 mV s^{-1} only led to a negligible change in polarization curves (Fig. S9), indicating efficient charge/mass transport and fast kinetics of the HzOR. To further scrutinize the electrocatalytic activity of Ru/α-MnO₂ and α-MnO₂, we compared the LSV curves of samples, acquired in 0.05 M H₂SO₄ electrolyte in the absence and presence of 0.5 M N₂H₄. In the absence of N₂H₄, both samples exhibit mediocre acidic OER performance, requiring a large overpotential to reach a current density of 10 mA cm^{-2} (Fig. 3b). After adding 0.5 M N₂H₄ into the electrolyte, the HzOR takes place much earlier than the OER, leading to a significant negative shift of the anodic onset potential for both samples. In particular, Ru/α-MnO₂ can deliver 10 mA cm^{-2} at an anodic potential of only 0.166 V *vs.* RHE, 1.687 V lower than that for OER (1.853 V *vs.* RHE) to reach the same current density. Fig. 3c further compares the electrocatalytic HzOR and OER performance of Ru/
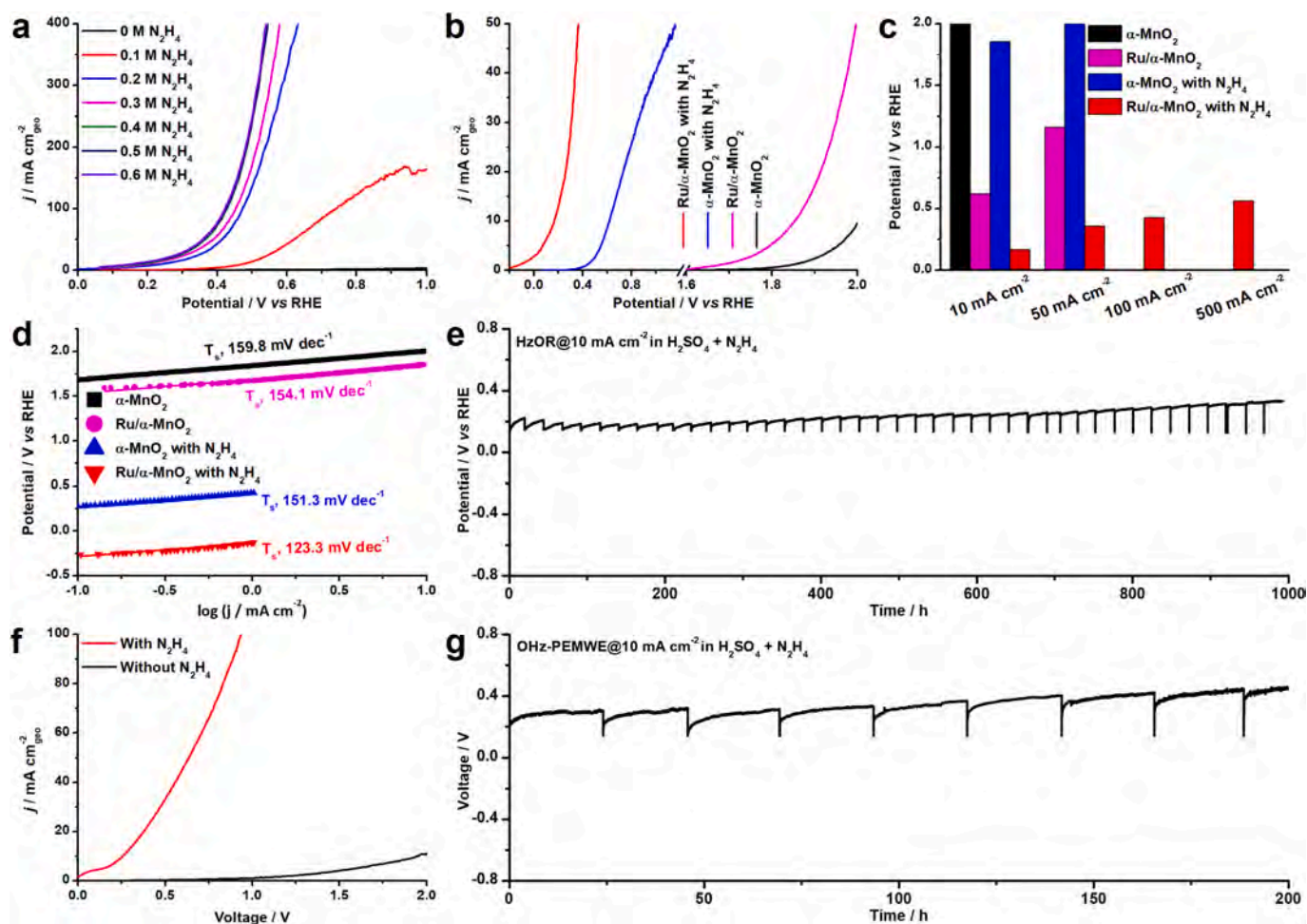
Fig. 3. Electrocatalytic performance of Ru/α-MnO$_2$. (a) The LSV curves measured in 0.05 M H$_2$SO$_4$ with different concentrations of N$_2$H$_4$. Scan rate: 5 mV s^{-1}. (b) Polarization curves of Ru/α-MnO$_2$ and α-MnO$_2$ catalysts in the absence and presence of 0.5 M N$_2$H$_4$. (c) Anodic potential comparison of Ru/α-MnO$_2$ and α-MnO$_2$ catalysts at various current densities in 0.05 M H$_2$SO$_4$ with and without the addition of 0.5 M N$_2$H$_4$. (d) Tafel plots for HzOR and OER derived from the LSV curves. (e) Chronopotentiometric curves of Ru/α-MnO$_2$ for HzOR at a constant current density of 10 mA cm^{-2}. (f) Polarization curves of a Ru/α-MnO$_2$ || Pt/C electrolyzer measured in 0.05 M H$_2$SO$_4$ with and without 0.5 M N$_2$H$_4$. (g) Chronopotentiometric curve of the Ru/α-MnO$_2$ || Pt/C cell recorded at 10 mA cm^{-2} in 0.05 M H$_2$SO$_4$ + 0.5 M N$_2$H$_4$, for the overall hydrazine-mediated PEMWE (Ohz-PEMWE). The spikes in (e) and (g) correspond to the replenishment of the electrolyte.

α-MnO$_2$ and α-MnO$_2$ in the 0.05 M H$_2$SO$_4$ electrolyte with and without 0.5 M N$_2$H$_4$, where Ru/α-MnO$_2$ exhibits excellent catalytic activities, able to deliver a large current density of 500 mA cm^{-2} at an anodic potential of merely 0.564 V vs. RHE in the presence of 0.5 M N$_2$H$_4$, better than the α-MnO$_2$ catalyst tested under the same conditions, confirming the advantage of Ru doping.

The reaction kinetics of catalysts was evaluated by Tafel analysis (Fig. 3d). The Ru/α-MnO$_2$ catalyst shows a smaller Tafel slope of 123.3 mV dec^{-1} for HzOR, compared to itself toward OER and α-MnO$_2$ for both reactions, suggesting its more favorable catalytic kinetics toward HzOR (Fig. 3d). Electrochemical impedance spectroscopy (EIS) measurements also disclosed that Ru/α-MnO$_2$ exhibits a much smaller charge transfer resistance (R$_{ct}$), indicative of the rapid charge transfer process at the electrode/electrolyte interface (Fig. S10). To further assess the intrinsic catalytic activity, the ECSA of Ru/α-MnO$_2$ and α-MnO$_2$ was estimated by the electrochemical double-layer capacitance (C$_{dl}$) method (Fig. S11). The Ru/α-MnO$_2$ catalyst shows an ECSA (371.4 cm^2) much higher than α-MnO$_2$ (291.4 cm^2), implying that it has significantly more active sites exposed. Nevertheless, the Ru/α-MnO$_2$ catalyst still exhibits a larger specific activity than α-MnO$_2$ for both HzOR and OER (Fig. S12), corroborating its high intrinsic catalytic activity.

The long-term stability is a critically important indicator of electrocatalysts for practical applications in water electrolyzers. The durability

of Ru/α-MnO$_2$ catalysts toward HzOR was evaluated by chronopotentiometry in 0.05 M H$_2$SO$_4$ + 0.5 M N$_2$H$_4$ electrolyte (pH = 8.3). As shown in Fig. 3e, the Ru/α-MnO$_2$ catalyst is able to continuously catalyze HzOR at 10 mA cm^{-2} for at least 1000 h with minimal degradation, showing outstanding durability. Furthermore, the operational stability of the Ru/α-MnO$_2$ catalyst was tested at a higher current density of 100 mA cm^{-2} in the same electrolyte. The HzOR can be accomplished stably under a low potential of 0.428 V for 220 h (Fig. S13), with only a slight increase in potential in the beginning of the test. Additionally, we performed post-mortem XPS and TEM analyses of the Ru/α-MnO$_2$ catalysts after the extended HzOR stability test at 10 mA cm^{-2} (Fig. S14). The Mn2p and Ru3p XPS spectra of Ru/α-MnO$_2$ after the durability test (Fig. S14a and S14b) reveal that the valence states of Mn and Ru in Ru/α-MnO$_2$ kept almost unchanged after the HzOR. Fig. S14c and S14d show that the NR-like microstructure was well retained but some ultrafine clusters with sub-nanometric sizes appeared alongside the Ru atom arrays. The above results demonstrate that adding hydrazine into the electrolyte can remarkably shift the anodic oxidation potential negatively, reducing the electrical energy input for hydrogen production; more importantly, it enables excellent operational stability given that hydrazine will neutralize the strong acid leading to a less aggressive oxidation environment, which in conjunction with the low working potential make Ru/α-MnO$_2$ remain electrochemically stable in

a long term.

Considering the superior catalytic activity and long-term stability of the Ru/α-MnO$_2$ catalyst toward HzOR, a two-electrode electrolyzer using Ru/α-MnO$_2$ as the anode catalysts and commercial Pt/C as the cathode catalysts has been assembled, with a proton exchange membrane (PEM) in between. The mixture of 0.05 M H$_2$SO$_4$ + 0.5 M N$_2$H$_4$ was employed as the electrolyte in both anodic and cathodic compartments. The Ru/α-MnO$_2$ || Pt/C pair can deliver geometric current densities of 10 and 100 mA cm^{-2} at votages of 0.254 V (E_{10}) and 0.935 V (E_{100}), respectively, in the presence of N$_2$H$_4$, significantly lower than the performance of the same electrode pair measured in 0.05 M H$_2$SO$_4$ without N$_2$H$_4$ (E_{10} = 1.948 V) (Fig. 3f). Additionally, the volume ratio of H$_2$ over N$_2$ is close to 2:1 and the Faradaic efficiency of the overall reaction is nearly 100% (Fig. S15). Besides, the Ru/α-MnO$_2$ || Pt/C pair also demonstrates outstanding long-term durability for the HzOR-assisted water electrolysis, able to produce H$_2$ at 10 mA cm^{-2} for 200 h without notable degradation (Fig. 3g). More importantly, the electrolysis can be accomplished stably at a higher current density of 100 mA cm^{-2} for at least 120 h (Fig. S16). It was noted that as the HER went

on, we did not detect obvious pH difference between the cathodic and anodic compartments within a few hours, likely because the protons consumed at the cathode can be compensated by the PEM.

Furthermore, we confirm that the HzOR and OHz-PEMWE can also be accomplished using Ru/α-MnO$_2$ as the anode catalysts in weak acid electrolyte (i.e., 0.225 M H$_2$SO$_4$ + 0.5 M N$_2$H$_4$, pH = 5.9). In this case, the Ru/α-MnO$_2$ can deliver geometric current densities of 10 and 100 mA cm$_{geo}^{-2}$ at potentials of 0.325 V and 0.627 V *vs.* RHE, respectively, still showing good catalytic activity (Fig. S17a) and stability (100 h @ 10 mA cm^{-2} without degradation, Fig. S17b). Besides, the OHz-PMEWE based on the Ru/α-MnO$_2$ || Pt/C pair is able to be achieved with small cell voltages of 0.491 V (E_{10}) and 1.145 V (E_{100}) at current densities of 10 and 100 mA cm^{-2} (Fig. S17c), respectively, exhibiting a favorable feature in energy-saving.

To gain a fundamental understanding of the enhanced HzOR catalytic activity, we further investigated the hydrazine oxidation processes on the pristine α-MnO$_2$, perfect Ru/α-MnO$_2$ and Ru/α-MnO$_2$ containing vacancies (defects) using density functional theory (DFT) calculations (Fig. S18). As shown in Fig. 4a, the hydrazine oxidation process usually
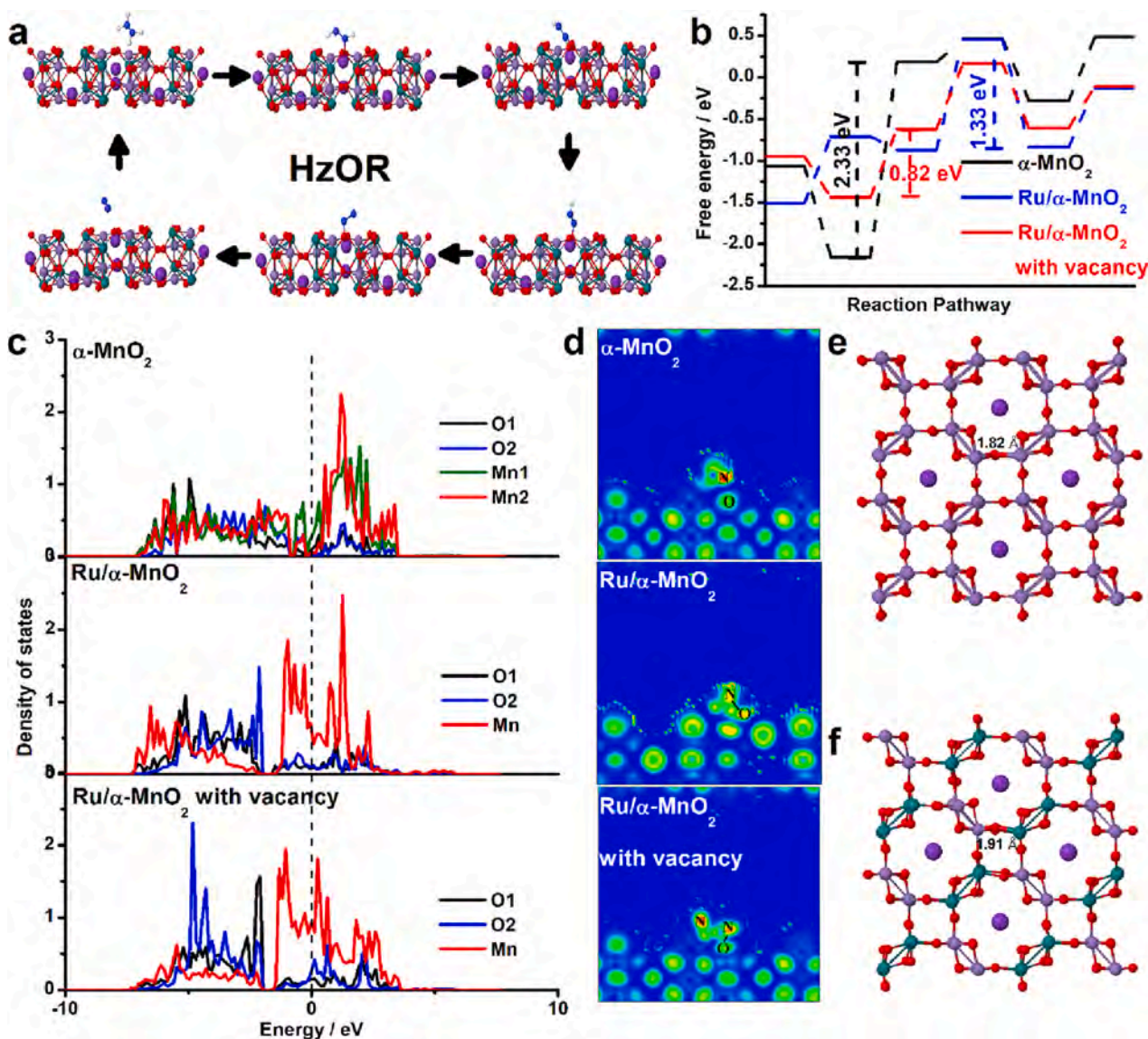

Fig. 4. Computational analyses of the Ru/α-MnO$_2$ for HzOR. (a) The proposed HzOR reaction steps. (b) The Gibbs free energy diagrams for the six reaction steps of HzOR. (c) PDOS and (d) ELF analyses of the α-MnO$_2$, Ru/α-MnO$_2$ and Ru/α-MnO$_2$ with vacancy configurations. The optimized unit cell structures of (e) α-MnO$_2$ and (f) Ru/α-MnO$_2$ showing the bond length. The purple, lavender, green and red spheres represent K, Mn, Ru and O atoms, respectively, in all models. (For interpretation of the references to colour in this figure legend, the reader is referred to the web version of this article.)

involves the adsorption of hydrazine molecules and the following four consecutive dehydrogenation steps (i.e., $*N_2H_4 \rightarrow *N_2H_3 \rightarrow *N_2H_2 \rightarrow *N_2H \rightarrow *N_2$). Therefore, the Gibbs free energies of the above catalyst models during the HzOR were calculated (Fig. 4b). The results show that the potential determining step (PDS) in the four-electron process for α-MnO$_2$ support is $*N_2H_3 \rightarrow *N_2H_2 + H^+ + e^-$, with a relatively high energy barrier of 2.33 eV [72]. For Ru/α-MnO$_2$, the PDS has been altered to the fourth elementary step ($*N_2H_2 \rightarrow *N_2H + H^+ + e^-$) with a much lower energy barrier of 1.33 eV, suggesting that Ru doping reinforce the adsorption strength of the $*N_2H_2$ intermediates and significantly improve the HzOR performance. Introducing cationic vacancy further helps decrease the barrier to 0.82 eV, demonstrating that under-coordination can accelerate the adsorption kinetics, thus boosting the intrinsic activity of HzOR.

The projected density of states (PDOS) was calculated to study the change in electronic properties after the introduction of Ru and vacancy. As shown in Fig. 4c, the Ru/α-MnO$_2$ with vacancy shows a larger PDOS near the Fermi level, compared to the pristine α-MnO$_2$ and perfect Ru/α-MnO$_2$, which can lead to a higher intrinsic electrical conductivity and provide more charge carriers for the catalytic reaction, boosting charge transfer kinetics. To further investigate the electronic interaction between the catalyst and the reactant/intermediates, we analyzed the electron localization function (ELF). While for α-MnO$_2$, the N atom in the reactant/intermediates does not tend to adsorb on the catalyst forming a bond with O, a bonding state between N and O can be notably observed in Ru/α-MnO$_2$ (Fig. 4d). However, this bond is so strong that it is not conducive to desorption, which would result in a higher activation energy. In comparsion, the Ru/α-MnO$_2$ with vacancy shows a moderate bonding strength, and thus has a better HzOR activity than perfect Ru/α-MnO$_2$. The optimized unit cell structures of α-MnO$_2$ and Ru/α-MnO$_2$ are displayed in Fig. 4e and f. The distance between O and Mn atoms increases from 1.82 to 1.91 Å after the original Mn atoms are replaced by Ru atoms. The Mn–O bonds show a tendency of being elongated, and the opposite is observed for the Ru–O bonds, consistent with previous Raman spectroscopy and EXAFS results (Fig. 2 and S5). This likely facilitates the generation of cationic defects, thus promoting the catalytic activity. Overall, our comprehensive DFT calculations revealed that Ru doping and the introduced vacancy increase the inherent conductivity and charge concentration of the catalyst and render a moderate adsorption energy between the catalysts and reactant/intermediates, thus synergistically enhancing the HzOR activity. The theoretical analyses support our experimental results consistently.

4. Conclusions

In summary, we report that Ru-doped α-MnO$_2$ nanorod catalysts show excellent electrocatalytic performance toward HzOR via proton exchange membranes and we further demonstrate that the HzOR-mediated overall water electrolysis can be carried out in near-neutral electrolytes to produce H$_2$, with significantly reduced cell voltage and good long-term stability, even at a large current density. Our comprehensive theoretical and experimental analyses reveal that Ru doping and the resultant cationic defects may elongate the Mn–O bond and alter the electronic structure of catalysts and thereby the interaction between catalysts and reactant/intermediates, thus reducing the overpotential and accelerating the reaction. The use of Ru/α-MnO$_2$ for the anodic HzOR completely eliminates the need for Ir-based materials to catalyze the OER in PEMWE, and moreover, the coupling of HzOR and HER substantially lowers the demand for electrical energy that accounts for a large amount of H$_2$ production cost, holding great promise for use in future green hydrogen production.

Declaration of Competing Interest

The authors declare that they have no known competing financial interests or personal relationships that could have appeared to influence the work reported in this paper.

Data availability

Data will be made available on request.

Appendix A. Supplementary data

Supplementary data to this article can be found online at https://doi.org/10.1016/j.cej.2023.144050.

References

[1] I. Staffell, D. Scamman, A. Velazquez Abad, P. Balcombe, P.E. Dodds, P. Ekins, N. Shah, K.R. Ward, The role of hydrogen and fuel cells in the global energy system, Energy Environ. Sci. 12 (2) (2019) 463–491.
[2] A. Buttler, H. Spliethoff, Current status of water electrolysis for energy storage, grid balancing and sector coupling via power-to-gas and power-to-liquids: A review, Renew. Sust. Energ. Rev. 82 (2018) 2440–2454.
[3] Z. Yu, Y. Li, A. Torres-Pinto, A.P. LaGrow, V.M. Diaconescu, L. Simonelli, M.J. Sampaio, O. Bondarchuk, I. Amorim, A. Araujo, A.M.T. Silva, C.G. Silva, J.L. Faria, L. Liu, Single-atom Ir and Ru anchored on graphitic carbon nitride for efficient and stable electrocatalytic/photocatalytic hydrogen evolution, Appl. Catal. B Environ., 310 (2022) 121318.
[4] X. Li, X. Hao, A. Abudula, G. Guan, Nanostructured catalysts for electrochemical water splitting: current state and prospects, J. Mater. Chem. A 4 (31) (2016) 11973–12000.
[5] Z. Yu, J. Xu, Y. Li, B. Wei, N. Zhang, Y. Li, O. Bondarchuk, H. Miao, A. Araujo, Z. Wang, J.L. Faria, Y. Liu, L. Liu, Ultrafine oxygen-defective iridium oxide nanoclusters for efficient and durable water oxidation at high current densities in acidic media, J. Mater. Chem. A 8 (46) (2020) 24743–24751.
[6] M. Carmo, D.L. Fritz, J. Mergel, D. Stolten, A comprehensive review on PEM water electrolysis, Int. J. Hydrogen Energy 38 (12) (2013) 4901–4934.
[7] N.-T. Suen, S.-F. Hung, Q. Quan, N. Zhang, Y.-J. Xu, H.M. Chen, Electrocatalysis for the oxygen evolution reaction: recent development and future perspectives, Chem. Soc. Rev. 46 (2) (2017) 337–365.
[8] Z. Yu, C. Si, F.J. Escobar-Bedia, A.P. LaGrow, J. Xu, M.J. Sabater, I. Amorim, A. Araujo, J.P.S. Sousa, L. Meng, J.L. Faria, P. Concepcion, B.o. Li, L. Liu, Bifunctional atomically dispersed ruthenium electrocatalysts for efficient bipolar membrane water electrolysis, Inorg. Chem. Front. 9 (16) (2022) 4142–4150.
[9] J. Xu, J. Li, Z. Lian, A. Araujo, Y. Li, B. Wei, Z. Yu, O. Bondarchuk, I. Amorim, V. Tileli, B.o. Li, L. Liu, Atomic-Step Enriched Ruthenium-Iridium Nanocrystals Anchored Homogeneously on MOF-Derived Support for Efficient and Stable Oxygen Evolution in Acidic and Neutral Media, ACS Catal. 11 (6) (2021) 3402–3413.
[10] L.i. An, C. Wei, M. Lu, H. Liu, Y. Chen, G.G. Scherer, A.C. Fisher, P. Xi, Z.J. Xu, C.-H. Yan, Recent Development of Oxygen Evolution Electrocatalysts in Acidic Environment, Adv. Mater. 33 (20) (2021) 2006328.
[11] M. Chatti, J.L. Gardiner, M. Fournier, B. Johannessen, T. Williams, T. R. Gengenbach, N. Pai, C. Nguyen, D.R. MacFarlane, R.K. Hocking, A.N. Simonov, Intrinsically stable in situ generated electrocatalyst for long-term oxidation of acidic water at up to 80 °C, Nat. Catal. 2 (2019) 457–465.
[12] C. Minke, M. Suermann, B. Bensmann, R. Hanke-Rauschenbach, Is iridium demand a potential bottleneck in the realization of large-scale PEM water electrolysis? Int. J. Hydrogen Energy 46 (46) (2021) 23581–23590.
[13] J. Xu, Z. Lian, B. Wei, Y. Li, O. Bondarchuk, N. Zhang, Z. Yu, A. Araujo, I. Amorim, Z. Wang, B.o. Li, L. Liu, Strong Electronic Coupling between Ultrafine Iridium-Ruthenium Nanoclusters and Conductive, Acid-Stable Tellurium Nanoparticle Support for Efficient and Durable Oxygen Evolution in Acidic and Neutral Media, ACS Catal. 10 (6) (2020) 3571–3579.
[14] A. Grimaud, A. Demortière, M. Saubanère, W. Dachraoui, M. Duchamp, M.-L. Doublet, J.-M. Tarascon, Activation of surface oxygen sites on an iridium-based model catalyst for the oxygen evolution reaction, Nat. Energy 2 (2016) 16189.

[15] T. Reier, M. Oezaslan, P. Strasser, Electrocatalytic Oxygen Evolution Reaction (OER) on Ru, Ir, and Pt Catalysts: A Comparative Study of Nanoparticles and Bulk Materials, ACS Catal. 2 (8) (2012) 1765–1772.

[16] A. Li, H. Ooka, N. Bonnet, T. Hayashi, Y. Sun, Q. Jiang, C. Li, H. Han, R. Nakamura, Stable Potential Windows for Long-Term Electrocatalysis by Manganese Oxides Under Acidic Conditions, Angew. Chem. Int. Ed. 58 (15) (2019) 5054–5058.

[17] A. Li, S. Kong, C. Guo, H. Ooka, K. Adachi, D. Hashizume, Q. Jiang, H. Han, J. Xiao, R. Nakamura, Enhancing the stability of cobalt spinel oxide towards sustainable oxygen evolution in acid, Nat. Catal. 5 (2022) 109–118.

[18] Z. Li, Y. Yan, S.-M. Xu, H. Zhou, M. Xu, L. Ma, M. Shao, X. Kong, B. Wang, L. Zheng, H. Duan, Alcohols electrooxidation coupled with H2 production at high current densities promoted by a cooperative catalyst, Nat. Commun. 13 (2022) 147.

[19] Y. Li, X. Wei, L. Chen, J. Shi, M. He, Nickel-molybdenum nitride nanoplate electrocatalysts for concurrent electrolytic hydrogen and formate productions, Nat. Commun. 10 (2019) 5335.

[20] D.T. Tran, T.H. Nguyen, H. Jeong, P.K.L. Tran, D. Malhotra, K.U. Jeong, N.H. Kim, J.H. Lee, Recent engineering advances in nanocatalysts for NH3-to-H2 conversion technologies, Nano Energy, 94 (2022) 106929.

[21] M. Zhang, H. Li, X. Duan, P. Zou, G. Jeerh, B. Sun, S. Chen, J. Humphreys, M. Walker, K. Xie, S. Tao, An Efficient Symmetric Electrolyzer Based On Bifunctional Perovskite Catalyst for Ammonia Electrolysis, Adv. Sci. 8 (22) (2021) 2101299.

[22] Z. Yu, Y. Li, V. Martin-Diaconescu, L. Simonelli, J. Ruiz Esquius, I. Amorim, A. Araujo, L. Meng, J.L. Faria, L. Liu, Highly Efficient and Stable Saline Water Electrolysis Enabled by Self-Supported Nickel-Iron Phosphosulfide Nanotubes With Heterointerfaces and Under-Coordinated Metal Active Sites, Adv. Funct. Mater. 32 (38) (2022) 2206138.

[23] Z.-Y. Yu, C.-C. Lang, M.-R. Gao, Y.u. Chen, Q.-Q. Fu, Y.u. Duan, S.-H. Yu, Ni–Mo–O nanorod-derived composite catalysts for efficient alkaline water-to-hydrogen conversion via urea electrolysis, Energy Environ. Sci. 11 (7) (2018) 1890–1897.

[24] Z. Yu, J. Xu, L. Meng, L. Liu, Efficient hydrogen production by saline water electrolysis at high current densities without the interfering chlorine evolution, J. Mater. Chem. A 9 (39) (2021) 22248–22253.

[25] Q. Liu, X. Liao, Y. Tang, J. Wang, X. Lv, X. Pan, R. Lu, Y. Zhao, X.-Y. Yu, H.B. Wu, Low-coordinated cobalt arrays for efficient hydrazine electrooxidation, Energy Environ. Sci. 15 (8) (2022) 3246–3256.

[26] Y. Zhu, J. Zhang, Q. Qian, Y. Li, Z. Li, Y. Liu, C. Xiao, G. Zhang, Y. Xie, Dual Nanoislands on Ni/C Hybrid Nanosheet Activate Superior Hydrazine Oxidation-Assisted High-Efficiency H2 Production, Angew. Chem. Int. Ed. 61 (2022) e202113082.

[27] F. Sun, J. Qin, Z. Wang, M. Yu, X. Wu, X. Sun, J. Qiu, Energy-saving hydrogen production by chlorine-free hybrid seawater splitting coupling hydrazine degradation, Nat. Commun. 12 (2021) 4182.

[28] Q. Qian, J. Zhang, J. Li, Y. Li, X. Jin, Y. Zhu, Y. Liu, Z. Li, A. El-Harairy, C. Xiao, G. Zhang, Y. Xie, Artificial Heterointerfaces Achieve Delicate Reaction Kinetics towards Hydrogen Evolution and Hydrazine Oxidation Catalysis, Angew. Chem. Int. Ed. 60 (2021) 5984–5993.

[29] S. Zhou, Y. Zhao, R. Shi, Y. Wang, A. Ashok, F. Héraly, T. Zhang, J. Yuan, Vacancy-Rich MXene-Immobilized Ni Single Atoms as a High-Performance Electrocatalyst for the Hydrazine Oxidation Reaction, Adv. Mater. 34 (2022) 2204388.

[30] Y. Li, X. Wei, S. Han, L. Chen, J. Shi, MnO2 Electrocatalysts Coordinating Alcohol Oxidation for Ultra-Durable Hydrogen and Chemical Productions in Acidic Solutions, Angew. Chem. Int. Ed. 60 (2021) 21464–21472.

[31] Y. Li, X. Wei, L. Chen, J. Shi, Electrocatalytic Hydrogen Production Trilogy, Angew. Chem. Int. Ed. 60 (2021) 19550–19571.

[32] Q. Yang, B. Zhu, F. Wang, C. Zhang, J. Cai, P. Jin, L. Feng, Ru/NC heterointerfaces boost energy-efficient production of green H2 over a wide pH range, Nano Research 15 (2022) 5134–5142.

[33] X. Liu, L. Zhang, Y. Zheng, Z. Guo, Y. Zhu, H. Chen, F. Li, P. Liu, B. Yu, X. Wang, J. Liu, Y. Chen, M. Liu, Uncovering the Effect of Lattice Strain and Oxygen Deficiency on Electrocatalytic Activity of Perovskite Cobaltite Thin Films, Adv. Sci. 6 (2019) 1801898.

[34] L. Simonelli, C. Marini, W. Olszewski, M. Ávila Pérez, N. Ramanan, G. Guilera, V. Cuartero, K. Klementiev, CLÆSS: The hard X-ray absorption beamline of the ALBA CELLS synchrotron, Cogent, Physics 3 (2016) 1231987.

[35] D.C. Koningsberger, R. Prins, X-ray absorption: principles, applications, techniques of EXAFS, SEXAFS, and XANES, John Wiley and Sons, New York, NY, United States, 1988.

[36] G. Bunker, Introduction to XAFS: A Practical Guide to X-ray Absorption Fine Structure Spectroscopy, Cambridge University Press, Cambridge, 2010.

[37] G. Kresse, J. Hafner, Ab initio molecular dynamics for liquid metals, Phys. Rev. B 47 (1) (1993) 558–561.

[38] G. Kresse, J. Furthmüller, Efficiency of ab-initio total energy calculations for metals and semiconductors using a plane-wave basis set, Comput. Mater. Sci. 6 (1) (1996) 15–50.

[39] P.E. Blöchl, Projector augmented-wave method, Phys. Rev. B 50 (24) (1994) 17953–17979.

[40] G. Kresse, D. Joubert, From ultrasoft pseudopotentials to the projector augmented-wave method, Phys. Rev. B 59 (3) (1999) 1758–1775.

[41] B. Hammer, L.B. Hansen, J.K. Nørskov, Improved adsorption energetics within density-functional theory using revised Perdew-Burke-Ernzerhof functionals, Phys. Rev. B 59 (1999) 7413–7421.

[42] I. Katsounaros, J.C. Meier, S.O. Klemm, A.A. Topalov, P.U. Biedermann, M. Auinger, K.J.J. Mayrhofer, The effective surface pH during reactions at the solid–liquid interface, Electrochem. Commun. 13 (2011) 634–637.

[43] J.A. Zamora Zeledón, A. Jackson, M.B. Stevens, G.A. Kamat, T.F. Jaramillo, Methods—A Practical Approach to the Reversible Hydrogen Electrode Scale, J. Electrochem. Soc. 169 (2022), 066505.

[44] C. Liu, M. Hirohara, T. Maekawa, R. Chang, T. Hayashi, C.-Y. Chiang, Selective electro-oxidation of glycerol to dihydroxyacetone by a non-precious electrocatalyst – CuO, Appl. Catal. B Environ. 265 (2020), 118543.

[45] C.C.L. McCrory, S. Jung, J.C. Peters, T.F. Jaramillo, Benchmarking Heterogeneous Electrocatalysts for the Oxygen Evolution Reaction, J. Am. Chem. Soc. 135 (2013) 16977–16987.

[46] L.R. Pahalagedara, S. Dharmarathna, C.K. King'ondu, M.N. Pahalagedara, Y.T. Meng, C.H. Kuo, S.L. Suib, Microwave-Assisted Hydrothermal Synthesis of α-MnO2: Lattice Expansion via Rapid Temperature Ramping and Framework Substitution, J. Phys. Chem. C 118 (2014) 20363–20373.

[47] C. Xie, D. Yan, H. Li, S. Du, W. Chen, Y. Wang, Y. Zou, R. Chen, S. Wang, Defect Chemistry in Heterogeneous Catalysis: Recognition, Understanding, and Utilization, ACS Catal. 10 (2020) 11082–11098.

[48] D. Yan, Y. Li, J. Huo, R. Chen, L. Dai, S. Wang, Defect Chemistry of Nonprecious-Metal Electrocatalysts for Oxygen Reactions, Adv. Mater. 29 (2017) 1606459.

[49] G. Wang, Y. Yang, D. Han, Y. Li, Oxygen defective metal oxides for energy conversion and storage, Nano Today 13 (2017) 23–39.

[50] Y. Zhu, W. Zhou, J. Yu, Y. Chen, M. Liu, Z. Shao, Enhancing Electrocatalytic Activity of Perovskite Oxides by Tuning Cation Deficiency for Oxygen Reduction and Evolution Reactions, Chem. Mater. 28 (2016) 1691–1697.

[51] K. Li, R. Zhang, R. Gao, G.-Q. Shen, L. Pan, Y. Yao, K. Yu, X. Zhang, J.-J. Zou, Metal-defected spinel MnxCo3-xO4 with octahedral Mn-enriched surface for highly efficient oxygen reduction reaction, Appl. Catal. B Environ. 244 (2019) 536–545.

[52] C.K. King'ondu, N. Opembe, C.-h. Chen, K. Ngala, H. Huang, A. Iyer, H.F. Garcés, S.L. Suib, Manganese Oxide Octahedral Molecular Sieves (OMS-2) Multiple Framework Substitutions: A New Route to OMS-2 Particle Size and Morphology Control, Adv. Funct. Mater. 21 (2) (2011) 312–323.

[53] M. Polverejan, J.C. Villegas, S.L. Suib, Higher Valency Ion Substitution into the Manganese Oxide Framework, J. Am. Chem. Soc. 126 (25) (2004) 7774–7775.

[54] L. Zhang, H. Jang, H. Liu, M.G. Kim, D. Yang, S. Liu, X. Liu, J. Cho, Sodium-Decorated Amorphous/Crystalline RuO2 with Rich Oxygen Vacancies: A Robust pH-Universal Oxygen Evolution Electrocatalyst, Angew. Chem. Int. Ed. 60 (34) (2021) 18821–18829.

[55] G. Liu, W. Li, R. Bi, C. Atangana Etogo, X.-Y. Yu, L. Zhang, Cation-Assisted Formation of Porous TiO2−x Nanoboxes with High Grain Boundary Density as Efficient Electrocatalysts for Lithium-Oxygen Batteries, ACS Catal. 8 (2018) 1720–1727.

[56] H. Han, H. Choi, S. Mhin, Y.-R. Hong, K.M. Kim, J. Kwon, G. Ali, K.Y. Chung, M. Je, H.N. Umh, D.-H. Lim, K. Davey, S.-Z. Qiao, U. Paik, T. Song, Advantageous crystalline–amorphous phase boundary for enhanced electrochemical water oxidation, Energy Environ. Sci. 12 (8) (2019) 2443–2454.

[57] Y.u. Duan, Z.-Y. Yu, S.-J. Hu, X.-S. Zheng, C.-T. Zhang, H.-H. Ding, B.-C. Hu, Q.-Q. Fu, Z.-L. Yu, X. Zheng, J.-F. Zhu, M.-R. Gao, S.-H. Yu, Scaled-Up Synthesis of Amorphous NiFeMo Oxides and Their Rapid Surface Reconstruction for Superior Oxygen Evolution Catalysis, Angew. Chem. Int. Ed. 58 (44) (2019) 15772–15777.

[58] C. Lin, J.-L. Li, X. Li, S. Yang, W. Luo, Y. Zhang, S.-H. Kim, D.-H. Kim, S.S. Shinde, Y.-F. Li, Z.-P. Liu, Z. Jiang, J.-H. Lee, In-situ reconstructed Ru atom array on α-MnO2 with enhanced performance for acidic water oxidation, Nat. Catal. 4 (2021) 1012–1023.

[59] J. Hou, Y. Li, L. Liu, L. Ren, X. Zhao, Effect of giant oxygen vacancy defects on the catalytic oxidation of OMS-2 nanorods, J. Mater. Chem. A 1 (2013) 6736–6741.

[60] F. Sabaté, J.L. Jordá, M.J. Sabater, A. Corma, Synthesis of isomorphically substituted Ru manganese molecular sieves and their catalytic properties for selective alcohol oxidation, J. Mater. Chem. A 8 (7) (2020) 3771–3784.

[61] F. Sabaté, J.L. Jordà, M.J. Sabater, Ruthenium isomorphic substitution into manganese oxide octahedral molecular sieve OMS-2: Comparative physic-chemical and catalytic studies of Ru versus abundant metal cationic dopants, Catal. Today 394–396 (2022) 414–424.

[62] F. Sabaté, M.J. Sabater, Recent Manganese Oxide Octahedral Molecular Sieves (OMS–2) with Isomorphically Substituted Cationic Dopants and Their Catalytic Applications, Catalysts 11 (2021) 1147.

[63] A. Doménech-Carbó, F. Sabaté, M.J. Sabater, Electrochemical Analysis of Catalytic and Oxygen Interfacial Transfer Effects on MnO2 Deposited on Gold Electrodes, J. Phys. Chem. C 122 (2018) 10939–10947.

[64] F. Sabaté, J. Navas, M.J. Sabater, A. Corma, Synthesis of γ-lactones from easily and accessible reactants catalyzed by Cu–MnOx catalysts, C. R. Chim. 21 (2018) 164–173.

[65] K. Wang, Y. Wang, B. Yang, Z. Li, X. Qin, Q. Zhang, L. Lei, M. Qiu, G. Wu, Y. Hou, Highly active ruthenium sites stabilized by modulating electron-feeding for sustainable acidic oxygen-evolution electrocatalysis, Energy Environ. Sci. 15 (2022) 2356–2365.

[66] J. Yin, J. Jin, M. Lu, B. Huang, H. Zhang, Y. Peng, P. Xi, C.-H. Yan, Iridium Single Atoms Coupling with Oxygen Vacancies Boosts Oxygen Evolution Reaction in Acid Media, J. Am. Chem. Soc. 142 (2020) 18378–18386.

[67] S. Chen, H. Huang, P. Jiang, K. Yang, J. Diao, S. Gong, S. Liu, M. Huang, H. Wang, Q. Chen, Mn-Doped RuO2 Nanocrystals as Highly Active Electrocatalysts for Enhanced Oxygen Evolution in Acidic Media, ACS Catal. 10 (2020) 1152–1160.

[68] M.C. Biesinger, B.P. Payne, A.P. Grosvenor, L.W.M. Lau, A.R. Gerson, R.S.C. Smart, Resolving surface chemical states in XPS analysis of first row transition metals, oxides and hydroxides: Cr, Mn, Fe, Co and Ni, Appl. Surf. Sci. 257 (7) (2011) 2717–2730.

[69] Y. Wen, P. Chen, L. Wang, S. Li, Z. Wang, J. Abed, X. Mao, Y. Min, C.T. Dinh, P.D. Luna, R. Huang, L. Zhang, L. Wang, L. Wang, R.J. Nielsen, H. Li, T. Zhuang,

C. Ke, O. Voznyy, Y. Hu, Y. Li, W.A. Goddard Iii, B. Zhang, H. Peng, E.H. Sargent, Stabilizing Highly Active Ru Sites by Suppressing Lattice Oxygen Participation in Acidic Water Oxidation, J. Am. Chem. Soc. 143 (2021) 6482–6490.

[70] Z. Shi, Y. Wang, J. Li, X. Wang, Y. Wang, Y. Li, W. Xu, Z. Jiang, C. Liu, W. Xing, J. Ge, Confined Ir single sites with triggered lattice oxygen redox: Toward boosted and sustained water oxidation catalysis, Joule 5 (2021) 2164–2176.

[71] J. Zheng, X. Peng, Z. Xu, J. Gong, Z. Wang, Cationic Defect Engineering in Spinel NiCo2O4 for Enhanced Electrocatalytic Oxygen Evolution, ACS Catal. 12 (2022) 10245–10254.

[72] M.T.M. Koper, Analysis of electrocatalytic reaction schemes: distinction between rate-determining and potential-determining steps, J. Solid State Electrochem. 17 (2013) 339–344.